

Dynamical crossover in the transient quench dynamics of short-range transverse field Ising models

Ceren B. Dağ* and Kai Sun

Department of Physics, University of Michigan, Ann Arbor, Michigan 48109, USA

(Dated: March 13, 2022)

Dynamical phase transitions (DPTs) are generally defined under two different but related categories: DPT-I where the equilibrium value, or long-time average, of the order parameter as a function of the control parameter demonstrates a phase boundary; DPT-II where the Loschmidt return rate shows a cusp singularity in real-time dynamics. Here we follow up on a recent numerical demonstration [Phys. Rev. Lett. 121, 016801 (2018)] where out-of-time-order correlators (OTOC) of a single-site are shown to exhibit DPT-I when quenched from polarized states both for integrable and nonintegrable short-range interacting transverse-field Ising model (TFIM). Given the requirement of sophisticated probe techniques to measure OTOC, we ask whether simpler single-site probes could be constructed to detect quantum phase transitions (QPT), e.g. magnetization per site. Quenched from polarized states, longitudinal magnetization has a featureless steady state regime in time for short-range TFIM, which prevents it from exhibiting DPT-I. Thus, we further question whether the transient regimes of such non-equilibrium processes could encode information about the underlying QPT. We show that the decay rates of time-dependent and single-site observables exhibit a cusplike feature, a reminiscent of the singularity in the integrable TFIM. The cusp separates two dynamical regimes, ordered and disordered, both of which have distinct nonequilibrium responses. We construct a dynamical order parameterlike quantity that exhibits a scaling law at the vicinity of the cusp. These signatures suggest a crossover behavior that is originated from the underlying QPT and encoded into the transient regime of one-point observables in short-range TFIM. When integrability is strongly broken, the crossover boundary turns into a region that separates two other dynamical regions that act like dynamically-ordered and -disordered regimes.

I. INTRODUCTION

Criticality, defined under Landau paradigm [1], is one of the milestones in our understanding of matter, providing us a framework to classify microscopically diverse phenomena in a handful of universality classes with their associated critical exponents [2, 3]. Its dynamical counterpart, dynamical criticality, studies both the imprints of equilibrium criticality on dynamics [4–14] and genuine non-equilibrium criticality that does not necessarily originate from an equilibrium transition [11, 12, 15–21]. Dynamical phase transitions (DPT) could in general be classified via two different but related definitions [11, 19, 22]: DPT-I and DPT-II. DPT-I is defined based on the time evolution of an (equilibrium) order parameter (OP) quenched from a state that is not an eigenstate of the evolution Hamiltonian [11]. In the ordered phase where the control parameter originates from the equilibrium transition, a prethermal regime appears with either equilibration or oscillatory saturation. Hence the long-time average of the signal could act like a dynamical OP, demonstrating a phase boundary. DPT-II concerns with cusp singularity appearing at critical times of the return rate that is based on Loschmidt echo and is linked to equilibrium phase transitions [9–11, 19, 22].

Recently out-of-time-order correlator (OTOC) of an arbitrary single-site observable (longitudinal magnetization per site) both for integrable and nonintegrable short-

range TFIM has been shown to exhibit DPT-I by Heyl et. al. [12], when quenched from polarized states. Given that measuring OTOCs requires sophisticated protocols such as reversing the overall sign of the Hamiltonian to realize backward time evolution [23, 24], or equally sophisticated alternative methods [25–27], in this paper we ask whether simpler single-site observables could be utilized to probe the underlying equilibrium quantum phase transition (QPT) of short-range TFIM in a quench protocol. Although DPT-I is well-defined for magnetization of the long-range TFIM [18, 19], there is no persistent dynamic order for short-range Hamiltonians, simply because the steady state regime of such global one-point observables, and likewise two-time correlators, is featureless [28–30]. Following [12], Ref. [21] showed that global two-point correlators (averaged over space) could exhibit DPT-I where the correlator acts like a dynamic OP, however here the correlator is not a single-site correlator unlike in Ref. [12]. In our paper, we focus on a single-site one-point observable (magnetization per site) that exhibits a featureless steady-state behavior similar to total magnetization in short-range TFIM, hence forbidding a DPT-I from being constructed.

The featureless steady-state for magnetization originates from the fact that this observable decays exponentially in time as both analytically and numerically studied in the integrable TFIM [28–33]. In fact exponential decay is also shown to exist in the XXZ model for magnetization [34]. Hence, we question whether the transient regime could encode information about the underlying equilibrium QPT. Such a question might also prove useful in laboratory implementations, given that it is challeng-

* cbdag@umich.edu

ing to reach steady-state regimes in experimental setups that are naturally coupled to an environment and experiences decoherence [35]. Ref. [34] previously showed that the decay parameter of the magnetization in the XXZ model shows a cusp between anti-ferromagnetic and XY-phases, when quenched from a Neel state. We first study the decay rates of single-site longitudinal magnetization in short-range TFIM with respect to the transverse field both for integrable and nonintegrable models; and observed that a similar cusplike feature emerges for the integrable TFIM. This is intuitive, due to the presence of singularities in short-range TFIM observed with transverse magnetization and quenched not only from ground states, but also from finite-temperature initial states [36]. However, we emphasize that we employ single-site longitudinal magnetization bounded by lightcones in their dynamics. Building on this knowledge, we study the scaling behavior at the vicinity of the cusplike structure and we find it to be logarithmic in the transverse field. The functional dependence of the decay rates on the transverse field at the vicinity of the cusp leads us to state the single-site magnetization in terms of transverse field, presenting us a dynamical scaling law at the vicinity of the cusp. Therefore we show that our rescaled single-site observable acts as a dynamic OP-like quantity. Although we work with single-site magnetization observables just like Ref. [12], unlike them we do not work in a steady-state regime where the observable could act as a dynamic OP for a DPT-I. Hence by working in the transient regime, we observe that one needs to rescale the dynamic observable with the scaling of the decay rates, which encodes information about the underlying QPT. Therefore, our results on the dynamical scaling laws of the rescaled single-site observable alongside the cusplike feature in the decay rates suggest a dynamical crossover that originates from the QPT.

Cusplike structure emerges at $h_c = 0.9999 \pm 0.0001$ for integrable TFIM with an associated scaling exponent $OP \sim h^\beta$ of $\beta = 1$ for the rescaled observable, separating two distinct nonequilibrium responses. These are, dynamically-ordered regime where the observable decays exponentially; and the dynamically-disordered regime where the observable shows an oscillatory exponential decay. The scaling trend of the rescaled observable is linear in the control parameter h , transverse-field, which is consistent with the presence of a cusplike structure. We note that the location of cusplike feature corresponds to the TFIM Hamiltonian that exhibits the fastest decay in the set of all Hamiltonians $H(h)$ with transverse fields at both sides of the equilibrium phase boundary. Given that observables cannot show divergent decay in short-range interacting systems due to lightcone bounds, it is reasonable that all decay rates are finite. Hence our data suggests a link between the fastest decay and the equilibrium QPT, confirming Ref. [34]. We use this observation to mark the boundary between dynamically-ordered and crossover regions in the nonintegrable TFIM. We break the integrability by introducing next-nearest neighbor

coupling to TFIM and study how the quench dynamics for single-site magnetization behave. After modeling the quench dynamics, we notice that three quantitatively distinct dynamical regimes emerge for the nonintegrable TFIM. The crossover boundary of the integrable TFIM enlarges into a region around the equilibrium QPT and separates two other dynamical regimes which act as -ordered and -disordered regimes of the integrable TFIM. This means that the nonintegrable TFIM exhibits a dominant trend of exponential decay in its dynamically-ordered regime; and a dominant trend of oscillatory exponential decay in its dynamically-disordered regime. We study the relevant decay rate and find that breaking integrability smooths out the cusplike structure (minimum) and shifts its location from the equilibrium phase boundary to $h_c = 2.278 \pm 0.001$. The minimum seems to separate the dynamically-ordered and crossover regions. The associated scaling exponent of the dynamical order parameterlike quantity reads $\beta \sim 2$, again consistent with the minimum of the decay rates.

In Sec. II, we introduce alternative temporal cutoffs to what is in use in the literature of DPT-I and focus on the dynamical crossover of the integrable TFIM. Then in Sec. III, we discuss how the method and the criteria defined in the previous section translates to nonintegrable TFIM. We conclude in Section V.

II. CROSSOVER IN TRANSIENT QUENCH DYNAMICS OF TFIM

In this paper, we work with TFIM with both nearest-neighbor (NN) and next-nearest-neighbor (NNN) couplings,

$$H = -J \sum_r^{N-1} \sigma_r^z \sigma_{r+1}^z - \Delta \sum_r^{N-2} \sigma_r^z \sigma_{r+2}^z + h \sum_r^N \sigma_r^x, \quad (1)$$

where σ_r^α are spin- $\frac{1}{2}$ Pauli spin matrices. TFIM preserves its gapped long range Ising ground state even when the interactions (or nonintegrability) Δ are introduced, although the transition boundary shifts to favor order as Δ increases. For all data in the paper, we fix $J = 1$ as the energy scale. Specifically we focus on the integrable model $\Delta/J = 0$ and nonintegrable model with $\Delta/J = -1$. Since we employ matrix product states (MPS) for large system sizes, we choose open boundary conditions and study the longitudinal magnetization at the middle of the chain $\sigma_{N/2}^z$. This site reproduces the decay dynamics of an arbitrary site in a periodic chain (Appendix A), and hence its decay is similar to the decay of total magnetization given that total magnetization is $M = 1/N \sum_r \sigma_r^z$. We study the dynamics of Eq. (1) $C(t) = \langle \psi_0 | \sigma_{N/2}^z(t) | \psi_0 \rangle$ quenched from a polarized state $|\psi_0\rangle = |\uparrow\uparrow \dots \uparrow\rangle$.

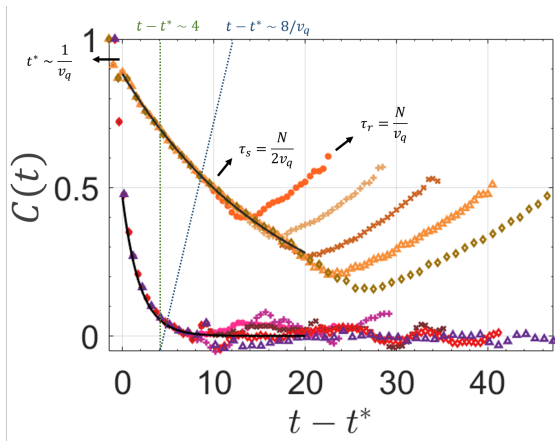


FIG. 1. $C(t)$ for $h/J = 0.5$ upper curves with orange tones and $h/J = 0.9$ lower curves with red tones. Each set of curves have system sizes between $N = 24$ (dots) and $N = 48$ (diamonds) denoted by different markers. τ_s and τ_r are separation and revival timescales (see text). x-axis is shifted with t^* , the reference time where the exponential decay starts. Green- and blue-dotted lines show two different temporal cutoffs applied in the study, fixed and parametric, respectively.

A. Temporal cutoffs

In DPT-I, one studies steady-state regime where the dynamics is expected to become independent of the time. Since such steady-state regimes might exhibit oscillatory behavior, typically due to finite-size effects in small systems, often times averaging over an interval of time is employed [9, 12, 21]. Averaging over a long interval of time also makes the dynamic OP to be less sensitive to where a temporal cutoff is applied in the steady-state regime. This is because oscillations could alter the dynamic OP if one only uses the value at the temporal cutoff. As a result, exact location of the temporal cutoff is not significant in the construction of the dynamical OP based on DPT-I as long as the temporal cutoff is in steady-state regime. A valid temporal cutoff that can be utilized in studying DPT-I is a system-size dependent cutoff, $t \sim \alpha N$ where the interval of time-averaging is proportional to the system size [19] up to a coefficient α .

This temporal cutoff does not work for one-point observables in short-range models, because as already mentioned before, these observables are featureless in their steady state regime, meaning that they decay exponentially to zero. If one were to use a cutoff $t \sim \alpha N$, we would simply observe a vanishing dynamic OP for one-point observables [12, 19] (see Appendix B). This observation aligns with the fact that one cannot construct DPT-I for magnetization in short-range TFIM. Hence, motivated on working in the transient regime, we turn our attention to the decay rates of the initial magnetization, which is known to exhibit a cusp at the QPT for the XXZ model [34]. In order to extract the exponential decay in the thermodynamic limit with finite-size systems,

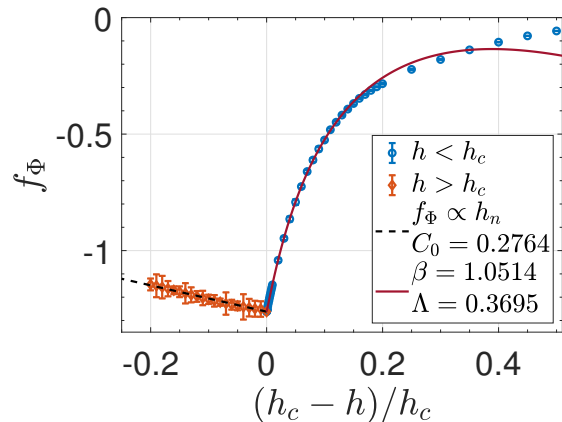


FIG. 2. Decay rates f_Φ for integrable TFIM in dynamically-ordered (blue-circles) and -disordered (red-diamonds) regimes. The dynamical transition is signaled by a cusplike structure at $h_c = 0.9999 \pm 0.0001$. Solid-red line is the logarithmic model to describe the ordered regime, whereas the black-dashed line is the linear model for disordered regime.

which are the only experimentally relevant systems, we find the lightcone bounds [29, 37, 38] on the magnetization per site for the finite sizes under study. The dynamics that remain in the lightcone exhibit exponential decay and do not show finite-size effects. Fig. 1 shows the integrable TFIM dynamics for $h/J = 0.5$ (orange tones) and $h/J = 0.9$ (red tones) for system sizes ranging between $N = 24$ (dots) and $N = 48$ (diamonds). In the lightcone, data for different system sizes collapse on each other while each separation point is roughly marked by $\tau_s = N/2v_q$ where v_q is the maximum quasi-particle velocity $v_q = \max|d\epsilon(h, k)/dk| = 2J\min(h, 1)$ [3, 29, 38]. τ_s is the time for the excitations caused by the quench to reach the end of the chain, and hence τ_s probes the size of the chain. When the chosen bulk spin is not at the middle of the chain its coefficient changes $\tau_s = \alpha/v_q$ where $N/2 \leq \alpha < N$. Revival timescale is marked by $\tau_r = N/v_q$, which is the time for the excitations to reflect back from the boundary to the middle of the chain. The timescale t^* is the short-distance cutoff of the temporal axis defined by the lattice constant divided by velocity $t^* \sim v_q^{-1}$. Here, t^* (τ_s) serves as the ultraviolet (infrared) cutoff, below (above) which the physics is dominated by non-universal microscopic details (finite-size effects). Thus, we focus on the (intermediate) time range $t^* < t < \tau_s$, where data of different system sizes collapse on each other and universal behavior arises as shown in Fig. 1 with an exponential decay [31–33]. The time interval that remains in the lightcone effectively simulates the decay in the thermodynamic limit.

Bounded by the lightcone, we find the decay rate of magnetization per site for an interval of transverse fields around the region that exhibits QPT in equilibrium. While the magnetization decays exponentially in the ordered regime, the exponential decay is

superposed with oscillations in the disordered regime $C(t) \sim \exp(f_\Phi t) \cos \omega t$, clearly differentiating two dynamic regimes from each other. Such an observation was made for the XXZ model in Ref. [34] and similarly we observe a cusplike feature in the decay rate f_Φ that points out to a crossover boundary. The boundary separates the dynamically-ordered regime (blue-circles) from -disordered regime (red-diamonds) in Fig. 2. The location of the crossover boundary reads $h_c = 0.9999 \pm 0.0001$. The decay rate in the ordered regime can be found as, $f_\Phi = \log(\gamma h_n^\beta \exp(-h_n/\Lambda) + C_0)$ (red-solid line in Fig. 2), where $h_n = (h_c - h)/h_c$ is the reduced control parameter, h_c is the crossover boundary, γ and β are free parameters to be found and Λ is the exponential cutoff coefficient which is explained below. We note that such a model for the decay rate is intuitive and explains the data in a large interval $0 < h_n \lesssim 0.5$, not only at the vicinity of the crossover. The constant C_0 points to the observation that the decay rate is never infinite, however the largest at the crossover boundary. Hence the system thermalizes the quickest at the crossover. Further C_0 is not a free parameter, but fixed by the data itself at the cusplike structure. Data follows $\log(\gamma h_n^\beta + C_0)$ at the vicinity of the crossover, while introducing an exponential cutoff [39] to the model lets us describe a bigger region of h_n as well as providing a definition for ‘vicinity of the crossover’, $h_n \ll \Lambda$.

One can measure the decay rates of magnetization at each transverse field and probe the cusplike feature as a way to detect the crossover. Alternatively, we aim to find a rescaling of the decaying observable that can render the rescaled observable a quantity that acts like a dynamical OP in the ordered regime right at the vicinity of the crossover. One can see this procedure as a way to construct a dynamical order parameterlike quantity with the correct rescaling that is originated from the scaling behaviour of the decay rates around the crossover. In DPT-I, the observable naturally acts as a dynamical OP in a nonzero valued steady-state. We find that for magnetization in short-range TFIM one needs to correctly rescale the observable to construct a quantity alike.

Similar to how a dynamical OP in DPT-I is constructed by first choosing a temporal cutoff, we consider two different temporal cutoffs applied at a time either (i) fixed $t \sim \text{constant}$ (green-dotted in Fig. 1) and (ii) parametric $t \sim \alpha v_q^{-1}$ (blue-dotted) where α is chosen so that the dynamic response remains in the lightcone. Eventually the rescaled dynamical OP-like quantity should not depend on how we choose our temporal cutoff. Furthermore, while one can average the observable for a time between the ultraviolet cutoff t^* and the chosen temporal cutoff t_L , this would complicate the functional form of the rescaling needed and it would require more data to compute/measure. Hence, we simply measure the observable $C(t)$ at time t_L dictated by the fixed or parametric temporal cutoff.

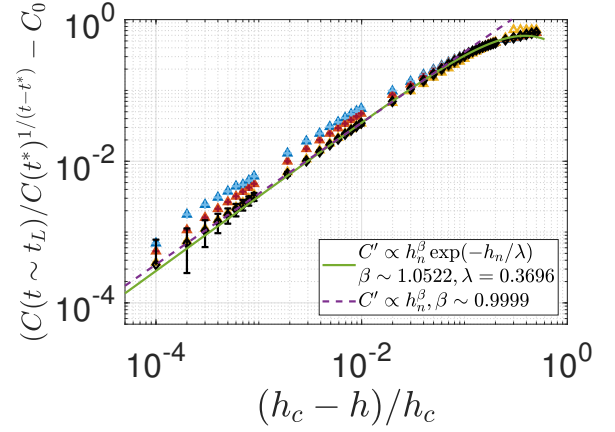


FIG. 3. The scaling at the vicinity of the crossover for integrable TFIM with respect to reduced control parameter h_n . y-axis is rescaled correctly to obtain the scaling (see text). The blue, red and yellow data are either fixed temporal cut-offs at times $t = 5.5, 4, 2.5$ (crosses) or parametric $t = \alpha v_q^{-1}$ with $\alpha = 11, 8, 5$ (triangles). Black-diamond line is data originated from the decay data analysis (see text). Purple-dashed line shows a power-law scaling with exponent $\beta = 1$ at the vicinity of the crossover while the green-solid line is power-law scaling with exponential cutoff to determine the vicinity of the crossover, $h_n \ll \Lambda = 0.37$.

B. Constructing a dynamical order parameterlike quantity

Let us rewrite the observable by substituting the scaling of the decay rate as a function of h ,

$$\begin{aligned} C(t) &= C(t^*) \exp(f_\Phi(t - t^*)) \\ &= C(t^*) (\gamma h_n^\beta \exp(-h_n/\Lambda) + C_0)^{t-t^*}. \end{aligned} \quad (2)$$

The scaling of the decay rate as a function of h_n reveals a scaling for the observable at the vicinity of the crossover $h_n \ll \Lambda$. This expression points out to the correct form of rescaling for the observable to make the procedure independent of the temporal cutoff. Hence the correct rescaling for the observable reads,

$$\left(\frac{C(t)}{C(t^*)} \right)^{1/(t-t^*)} - C_0 = \gamma h_n^\beta \exp(-h_n/\Lambda), \quad (3)$$

leading us to define a dynamical OP-like quantity,

$$C'(h_n) = \left(\frac{C(t)}{C(t^*)} \right)^{1/(t-t^*)} - C_0, \quad (4)$$

which is strictly valid at the vicinity of the crossover.

Fig. 3 shows how the dynamical OP-like quantity $C'(h_n)$ constructed based on different cutoffs scales with $h_n = (h_c - h)/h_c$ at the vicinity of the crossover. The colors yellow, red and blue correspond to cutoffs chosen at fixed $t_L = 2.5, 4, 5.5$ (plus markers) and at $\alpha = 5, 8, 11$ for parametric $t_L = \alpha/v_q$ (triangle markers). All data accumulate closely to each other and in particular data for different type temporal cutoffs collapse perfectly (Appendix

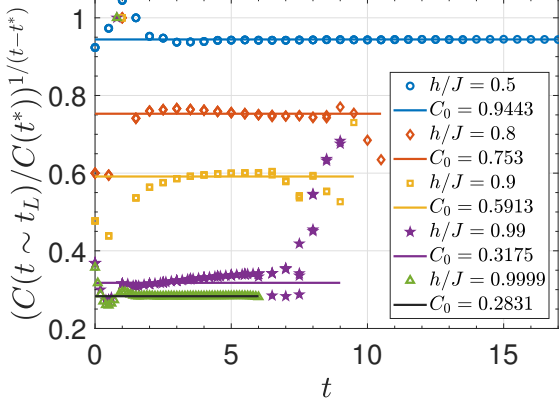


FIG. 4. Rescaled y-axis is plotted against time for different h/J up to constant C_0 (see legend). The solid flat lines are exponential model prediction while the data (markers) accumulates around them with slight divergences (see text).

C). The black-diamond line in Fig. 3 demonstrates the scaling of dynamical OP-like quantity based on the decay rates and it coincides with the data up to a small deviation for larger times. This deviation can be seen to be due to the inaccuracies in the numerical analysis. Fig. 4 demonstrates how the observable data (markers) could differ from a perfect exponential model which is denoted by the flat lines for some h/J (see legend). Note that the deviation is larger for larger times at the vicinity of the crossover and explains why we do not see a perfect collapse in Fig. 3. Fig. 4 also shows that ideally the rescaling of the observable renders the rescaled observable a constant of time. Thus, indeed in the ideal situation where there is no numerical inaccuracies, the rescaled observable is a function of only the reduced control parameter, $C'(h_n)$.

We obtain a linear scaling for the dynamical OP-like quantity $\propto h_n^\beta$ where $\beta = 0.9999$ when only the data at the vicinity of the crossover is used (purple-dotted line in Fig. 3). The vicinity of the crossover is found by first fitting the power-law scaling with an exponential cutoff, $h_n \ll \Lambda \sim 0.37$ which corresponds to $h \sim 0.96$ (green-solid line in Fig. 3). The linear scaling is consistent with the cusp at the dynamic crossover boundary.

In the dynamically-disordered regime, the decay rate is linear at the vicinity of the crossover, $f_\Phi \propto h_n$ as seen in red-diamonds line of Fig. 2. Since this regime is oscillatory, we study the angular frequency ω and observe that $\omega \propto (-h_n)^\delta$ where $\delta \sim 0.5$, marking $h_n = 0$ as the crossover boundary as well, consistently with the rest of our results.

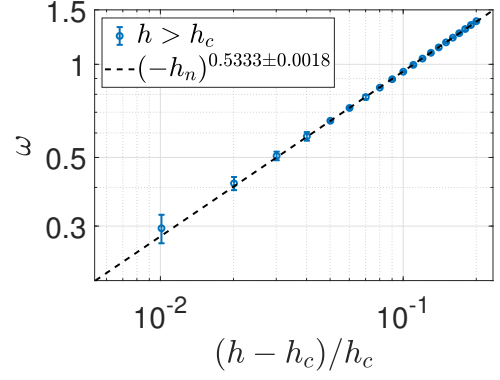


FIG. 5. Angular frequency scales with $-h_n$ with a power-law exponent of $\delta \sim 0.5$ in the disordered regime at the vicinity of the crossover.

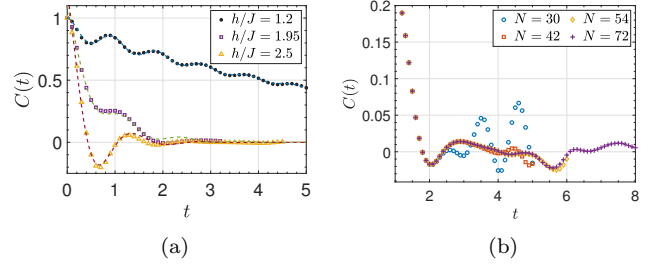


FIG. 6. (a) Nonintegrable TFIM with $\Delta/J = -1$ for different $h/J = 1.2, 1.95, 2.5$ and dashed lines are the minimal model predictions for dynamic responses. (b) One-point observable for nonintegrable TFIM $\Delta/J = -1$ at $h/J \sim 2$ with respect to time for different system sizes between $N = 30 - 72$.

III. DYNAMICAL CROSSOVER IN THE NONINTEGRABLE TFIM

Having studied the dynamical crossover observed in the transient regime for a noninteracting model, we now turn our attention nonintegrable TFIM.

We break the integrability of the model by taking $\Delta/J = -1$ in Eq. 1, which hosts an equilibrium QPT at $h_c \sim 2.46$ (Appendix D). Fig. 6a shows the sophisticated dynamic response of this model for different h values in the lightcone determined by data ranging from $N = 24$ to $N = 42$. Lightcones are determined similarly by studying the separation timescales τ_s of different system sizes. Fig. 6b shows the presence of well-defined τ_s timescales for a range of different system sizes at $h/J = 2$.

A. Minimal Model

An important difference from the noninteracting model is the oscillations existing in both dynamically-ordered and -disordered regimes. Hence, we first aim to approximately model the dynamic response. Since oscillations

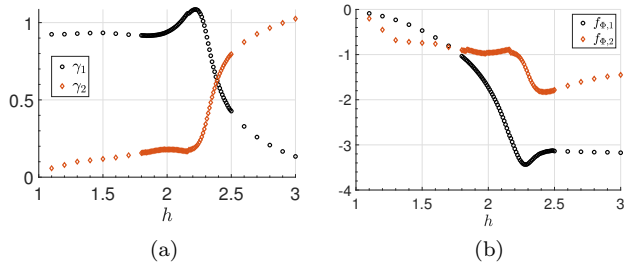


FIG. 7. (a) The coefficients γ_1 (black-circles) and γ_2 (orange-diamonds); (b) the decay rates $f_{\Phi,1}$ (black-circles) and $f_{\Phi,2}$ (orange-diamonds) of minimal model for the dynamics of non-integrable TFIM at $\Delta/J = -1$.

are present at every h/J , a minimal model that can reproduce the important features of the dynamics is,

$$C(t) = \gamma_1 \exp(f_{\Phi,1}t) + \gamma_2 \exp(f_{\Phi,2}t) \cos \omega t. \quad (5)$$

The dashed lines in Fig. 6a show how well the minimal model can describe the dynamics. The first and the second terms are analogous terms for the dynamically-ordered and -disordered regimes of the integrable TFIM, respectively. Thus, an immediate observation is that there seems no sharply distinct dynamical regimes as in integrable TFIM. We study the parameters γ_1 , γ_2 , $f_{\Phi,1}$ and $f_{\Phi,2}$ as a function of transverse field, which is depicted in Fig. 7.

By studying $\gamma_{1,2}$, coefficients of the terms, we first notice that the non-oscillatory term is dominant to the oscillatory term in the region $h \lesssim 2.3$. The opposite is true for $h \gtrsim 2.6$. Hence, even though there are not two distinct models that describe two distinct regimes like in integrable TFIM, there are two limits of one model that exhibit distinct enough features. This behaviour seems to stem from the cusplike crossover that is observed in the integrable model. This is because, the minimal model reduces to one term only where $\gamma_2 = 0$ in dynamically-ordered regime and $\gamma_1 = 0$ in the -disordered regime. In this sense, under minimal model integrable and nonintegrable models are quantitatively connected to each other. Note that $\gamma_{1,2}$ intersects at a location very close to the equilibrium QPT and this is where both terms are equally significant in the nonequilibrium response. Therefore, one can separate the entire region roughly into three: (1) $h \lesssim 2.3$ where the dynamics can be approximated by only the non-oscillatory term, and hence acts like the dynamically-ordered regime in the integrable TFIM. (3) $h \gtrsim 2.6$ where the dynamics can be approximated by only the oscillatory term, and hence acts like the dynamically-disordered regime in the integrable TFIM. (2) The intermediate crossover region where both terms are important.

The minimal model could be improved with larger system size data in the future studies to determine features of these parameters with greater accuracy. Additionally, testing the minimal model against nonintegrability

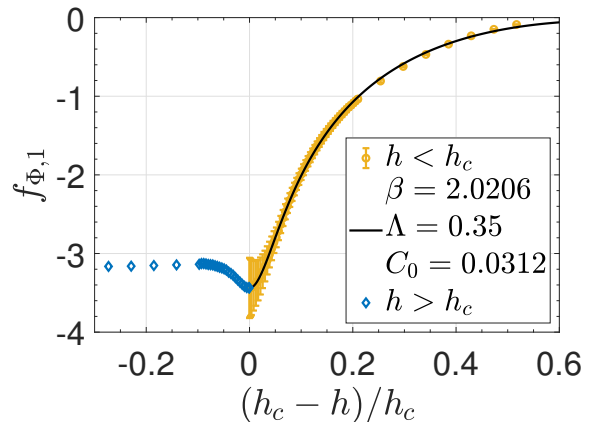


FIG. 8. Decay rate of the first term in minimal model Eq. (5), $f_{\Phi,1}$ shows a smooth cusp/minimum at $h_c = 2.278 \pm 0.001$ signaling a boundary between the ordered regime (yellow-circles) that can be modeled by logarithmic function (black-solid) and crossover region (blue-diamonds).

strength Δ/J is an interesting direction for future studies. In particular, it would be interesting to study how the regions (1) through (3) change in a near-integrability model. Finally let us note that although there might be other equally accurate models to represent the dynamics of nonintegrable TFIM, the current model has the least amount of free parameters and is physically intuitive.

B. Dynamical crossover region and an OP-like quantity

We focus on the decay rate of the first term, $f_{\Phi,1}$ since this is the term that governs the exponential decay of the dynamic response, whereas $f_{\Phi,2}$ controls the exponential decay of the oscillations. In this sense, $f_{\Phi,1}$ is the analogous parameter to the decay parameter in the integrable TFIM. In addition to the observation that the system thermalizes the fastest at the crossover boundary in the integrable TFIM, we notice that the minimum of $f_{\Phi,1}$ roughly coincides with the boundary between the dynamically-ordered (1) and the crossover (2) regions. Given that in the integrable TFIM, the cusplike structure emerges when the nonequilibrium response changes nature, it seems that the minimum of $f_{\Phi,1}$ implies a possible boundary between the regions (1) and (2). In this regard, region (1) is where the nonequilibrium response can be approximated well enough with an exponential decay only; and region (2) is where one cannot ignore the oscillatory term anymore.

Fig. 8 demonstrates this minimum for $f_{\Phi,1}$. We determine the location of the minimum as $h_c = 2.278 \pm 0.001$ which sets the boundary from dynamically-ordered (1) to the crossover (2) regions. The decay rate in the region (1) follows previously introduced logarithmic scaling in h_n (Fig. 8) giving rise Eq. 2 to hold for the nonintegrable

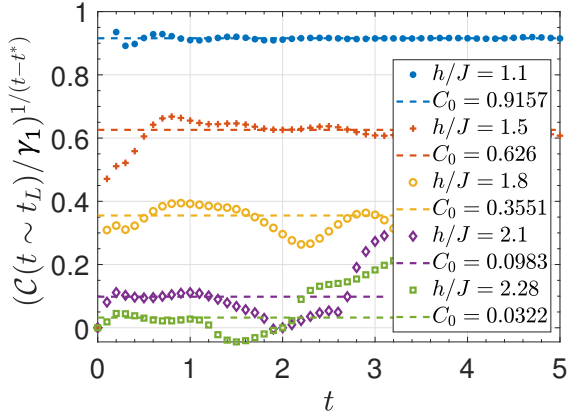


FIG. 9. Exponential model predictions shown with solid flat lines and rescaled observable data according to the method (i) (see text) around the flat lines for different h/J values.

model, as long as the oscillations are taken care of. This could be performed in a couple of different ways, e.g. averaging over a period $\mathcal{T} = 2\pi/\omega$, working only at the nodes of the oscillations $(\pi + 2\pi n)/2\omega$ where $n \in \mathbb{Z}$ or simply rescaling the observable by subtracting the oscillatory term from the observable data. Let us briefly discuss these options.

(i) The first method employed here in the main text is simple rescaling by subtracting the oscillatory term from $C(t) \rightarrow \mathcal{C}(t) = C(t) - \gamma_2 \exp(f_{\Phi,2}t) \cos(\omega t)$. Hence the rescaling of the observable $\mathcal{C}(t)$ follows similarly to Eq. (3). In such an expression, γ_1 , γ_2 , $f_{\Phi,2}$ and ω are free parameters. Fig. 9 demonstrates how well the rescaled data can be explained by an exponential decay when the observable is rescaled according to method (i). At the vicinity of the boundary, data coincides well with the flat lines in early times. Overall, the exponential model describes the general trend of the data in region (1).

(ii) The second method is to choose a temporal cutoff at the nodes of the oscillations. This introduces a condition on the temporal cutoff time t_L as

$$t_L = \frac{\pi + 2\pi n}{2\omega}, \quad n \in \mathbb{Z}.$$

For sufficiently long dynamical response, this condition is not restrictive. When the condition is satisfied, the rescaled observable reduces to Eq. (3) with only one free parameter γ_1 .

(iii) Finally one can think of averaging the observable data over a period of \mathcal{T} . Let us first discuss this case for the integrable TFIM. By a time-averaging integral over a period of \mathcal{T} around the temporal cutoff t_L , the result reads

$$\begin{aligned} & \frac{1}{\mathcal{T}} \int_{t_L - \mathcal{T}/2}^{t_L + \mathcal{T}/2} dt C(t^*) \exp[f_{\Phi}(t - t^*)] \\ &= C(t^*) \exp[f_{\Phi}(t - t^*)] \frac{\sinh(f_{\Phi}\mathcal{T}/2)}{f_{\Phi}\mathcal{T}/2}. \end{aligned}$$

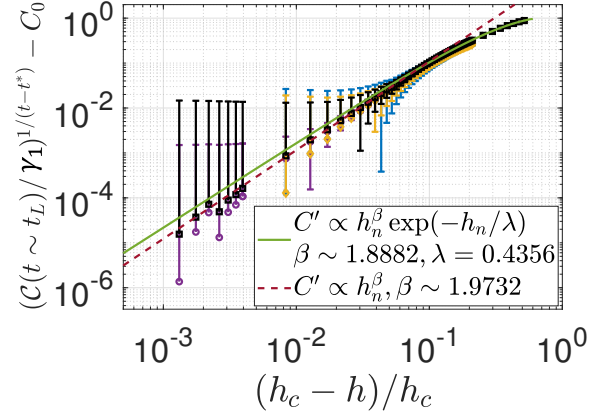


FIG. 10. Power-law dynamical scaling at the vicinity of the boundary between regions (1) and (2) with an exponent of $\beta \sim 2$ with blue and yellow data at very early times $t = 0.3, 0.5$ with the rescaling method (i) and purple data at the nodes of the oscillations motivated by the method (ii) (see text).

In the limit of $\mathcal{T} \rightarrow 0$, we recover the result with no averaging. We note that in case of averaging, one needs to rescale the observable correctly with the averaging interval \mathcal{T} as well in order to construct a dynamical OP-like quantity. Although a similar procedure can be applied for the nonintegrable model, this method requires fine-tuning of t_L and the averaging interval \mathcal{T} based on the free parameters ω and $f_{\Phi,2}$ to get rid of the oscillatory term in the minimal model. Even though there happens to be infinite number of possible pairs of temporal cutoff and averaging interval (t_L, \mathcal{T}) in total, there are conditions for viable sets (t_L, \mathcal{T}) which introduces fine-tuning. Since such a method is likely to be inconvenient both for computation and experiment, we do not discuss it further.

We plot the rescaled observable with temporal cutoff applied at $t = 0.3$ (blue) and $t = 0.5$ (yellow) in Fig. 10 in addition to data at a node of the oscillation with angular frequency ω (purple). The black-squares show the dynamical OP-like quantity derived from the decay rate, Fig. 8. All data collapses reasonably well and can be described by the power-law scaling of $\beta \sim 2$ at the vicinity $h_n \ll \Lambda = 0.44$, which corresponds to $h \sim 2.23$. The scaling exponent is consistent with the smooth and continuous crossover boundary. For details on the error bars, see Appendix E.

IV. DISCUSSIONS AND CONCLUSIONS

We studied the decay rates of single-site one-point observables, magnetization per site for (non-)integrable TFIM as a function of transverse field. The integrable TFIM exhibited cusplike feature in the decay rates at $h_c = 0.9999 \pm 0.0001$, suggesting a dynamical crossover

between dynamically-ordered and -disordered regimes. Although the magnetization per site for short-range TFIM decays exponentially and results in a featureless steady-state for DPT-I, we showed that cusplike structure in the decay rates separates two distinct nonequilibrium responses. In the dynamically-ordered regime, the observable exponentially decays to zero, whereas the nonequilibrium response is an exponential decay superposed with oscillations in the dynamically-disordered regime. By studying the scaling of the decay rates at the vicinity of the crossover, we found a rescaling for the observable and the rescaled observable exhibited a linear dynamical scaling law in the ordered vicinity of the crossover.

Next we wrote down a minimal model that fits the nonequilibrium behavior of the nonintegrable TFIM. Three regions appeared from the model where in (1) $h \lesssim 2.3$ the response is dominated by a smooth exponential decay and hence acting like a dynamically-ordered regime; (3) $h \gtrsim 2.6$ the response is dominated by an oscillatory exponential decay and hence acting like a dynamically-disordered regime; and (2) the intermediate crossover region where none of the terms can be ignored. Hence, we observe that the point-like crossover boundary in the integrable TFIM turns into a region in the nonintegrable model. It is an interesting direction to test this model, its parameters and the region boundaries against different Δ/J .

Later we focused on the decay rate of the non-oscillatory term which showed a minimum (a smoothed cusp) at the boundary between dynamically-ordered and crossover regions $h_c = 2.278 \pm 0.001$; and found a dynamical OP-like quantity based on simple temporal cut-offs in the transient regime that can probe this feature of the model after rescaling the observable. The rescaled observable exhibited a dynamical scaling law exponent $\beta \sim 2$.

Although we employ single-site observables that reproduces the results of the total magnetization which scales with the system size, our observable is still a local one with its response recorded in short times bounded by lightcones. This leads us to interpret our results in the context of a crossover even for the integrable TFIM, in-

stead of a transition. To rigorously argue for a transition, one could show a finite-size scaling of the cusp behaviour becoming sharper with increasing system size. Whether the observed cusplike feature points to a transition, and the dynamical regimes might actually be phases could be tested with larger system sizes and longer simulation times in the future. Even though the region remains in the lightcone effectively simulates the nonequilibrium response in the thermodynamic limit, there are still finite-size effects which are recently reported to be exponentially small in the system size [40]. For the nonintegrable TFIM, observed physics clearly point out to different manifestations of the same quantum phase connected by a smooth crossover. Nevertheless finite-size scaling analysis could be applied to the boundaries between the nonequilibrium regions. In fact studying larger system sizes for the nonintegrable models would provide larger time intervals remaining in the lightcone and thus improve the model that describes the data better, which in turn could lead to more precise and accurate predictions on these emerging regions of different nonequilibrium responses as a function of transverse field.

Our work opens new avenues to explore non-equilibrium order, in particular with local observables, with no need for reaching the saturation regime which might be challenging for experiments [35]. There are interesting directions for future, such as (i) whether a similar dynamical OP-like quantity could be constructed for other short-range Hamiltonians, e.g. the XXZ model; and (ii) whether long-range interacting TFIM [41] could exhibit similar behavior.

V. ACKNOWLEDGMENTS

We thank Jad C. Halimeh and L.-M. Duan for helpful suggestions and discussions. DMRG calculations are designed with ITensor [42] and performed by the Great Lakes High Performance Computing Cluster of the University of Michigan. This work was supported by National Science Foundation under Grant EFRI-1741618.

-
- [1] L. D. Landau, Zh. Eksp. Teor. Fiz. **7**, 19 (1937), [Phys. Z. Sowjetunion **11**, 26 (1937); Ukr. J. Phys. **53**, 25 (2008)].
 - [2] J. Zinn-Justin, *Quantum Field Theory and Critical Phenomena*; 4th ed., Internat. Ser. Mono. Phys. (Clarendon Press, Oxford, 2002).
 - [3] S. Sachdev, *Quantum Phase Transitions* (Cambridge University Press, 2001).
 - [4] W. H. Zurek, U. Dorner, and P. Zoller, Phys. Rev. Lett. **95**, 105701 (2005).
 - [5] B. Damski and W. H. Zurek, Phys. Rev. Lett. **99**, 130402 (2007).
 - [6] J. Dziarmaga, Advances in Physics **59**, 1063 (2010).
 - [7] A. Polkovnikov, K. Sengupta, A. Silva, and M. Vengalattore, Rev. Mod. Phys. **83**, 863 (2011).
 - [8] E. Nicklas, M. Karl, M. Höfer, A. Johnson, W. Muesel, H. Strobel, J. Tomkovič, T. Gasenzer, and M. K. Oberthaler, Phys. Rev. Lett. **115**, 245301 (2015).
 - [9] M. Heyl, A. Polkovnikov, and S. Kehrein, Phys. Rev. Lett. **110**, 135704 (2013).
 - [10] M. Heyl, Reports on Progress in Physics **81**, 054001 (2018).
 - [11] T. Mori, T. N. Ikeda, E. Kaminishi, and M. Ueda, Journal of Physics B: Atomic, Molecular and Optical Physics **51**, 112001 (2018).

- [12] M. Heyl, F. Pollmann, and B. Dóra, Phys. Rev. Lett. **121**, 016801 (2018).
- [13] C. B. Dağ, K. Sun, and L.-M. Duan, Phys. Rev. Lett. **123**, 140602 (2019).
- [14] B.-B. Wei, G. Sun, and M.-J. Hwang, Phys. Rev. B **100**, 195107 (2019).
- [15] M. Eckstein, M. Kollar, and P. Werner, Phys. Rev. Lett. **103**, 056403 (2009).
- [16] B. Sciolla and G. Biroli, Phys. Rev. B **88**, 201110 (2013).
- [17] N. Tsuji, M. Eckstein, and P. Werner, Phys. Rev. Lett. **110**, 136404 (2013).
- [18] J. C. Halimeh, V. Zauner-Stauber, I. P. McCulloch, I. de Vega, U. Schollwöck, and M. Kastner, Phys. Rev. B **95**, 024302 (2017).
- [19] B. Žunkovič, M. Heyl, M. Knap, and A. Silva, Phys. Rev. Lett. **120**, 130601 (2018).
- [20] J. Zhang, G. Pagano, P. W. Hess, A. Kyprianidis, P. Becker, H. Kaplan, A. V. Gorshkov, Z. X. Gong, and C. Monroe, Nature (London) **551**, 601 (2017), arXiv:1708.01044 [quant-ph].
- [21] P. Titum, J. T. Iosue, J. R. Garrison, A. V. Gorshkov, and Z.-X. Gong, Phys. Rev. Lett. **123**, 115701 (2019).
- [22] J. C. Halimeh and V. Zauner-Stauber, Phys. Rev. B **96**, 134427 (2017).
- [23] B. Swingle, G. Bentsen, M. Schleier-Smith, and P. Hayden, Phys. Rev. A **94**, 040302 (2016).
- [24] C. B. Dağ and L.-M. Duan, Phys. Rev. A **99**, 052322 (2019).
- [25] G. Zhu, M. Hafezi, and T. Grover, Phys. Rev. A **94**, 062329 (2016).
- [26] N. Y. Yao, F. Grusdt, B. Swingle, M. D. Lukin, D. M. Stamper-Kurn, J. E. Moore, and E. A. Demler, arXiv e-prints, arXiv:1607.01801 (2016), arXiv:1607.01801 [quant-ph].
- [27] B. Vermersch, A. Elben, L. M. Sieberer, N. Y. Yao, and P. Zoller, Phys. Rev. X **9**, 021061 (2019).
- [28] F. H. L. Essler, S. Evangelisti, and M. Fagotti, Phys. Rev. Lett. **109**, 247206 (2012).
- [29] P. Calabrese, F. H. L. Essler, and M. Fagotti, Journal of Statistical Mechanics: Theory and Experiment **2012**, P07016 (2012).
- [30] P. Calabrese, F. H. L. Essler, and M. Fagotti, Phys. Rev. Lett. **106**, 227203 (2011).
- [31] S. Sachdev and A. P. Young, Phys. Rev. Lett. **78**, 2220 (1997).
- [32] P. Calabrese and J. Cardy, Phys. Rev. Lett. **96**, 136801 (2006).
- [33] D. Rossini, A. Silva, G. Mussardo, and G. E. Santoro, Phys. Rev. Lett. **102**, 127204 (2009).
- [34] P. Barmettler, M. Punk, V. Gritsev, E. Demler, and E. Altman, Phys. Rev. Lett. **102**, 130603 (2009).
- [35] H.-X. Yang, T. Tian, Y.-B. Yang, L.-Y. Qiu, H.-Y. Liang, A.-J. Chu, C. B. Dağ, Y. Xu, Y. Liu, and L.-M. Duan, Phys. Rev. A **100**, 013622 (2019).
- [36] Y. Li, M. Huo, and Z. Song, Phys. Rev. B **80**, 054404 (2009).
- [37] E. H. Lieb and D. W. Robinson, Communications in Mathematical Physics **28**, 251 (1972).
- [38] P. Calabrese and J. Cardy, Journal of Statistical Mechanics: Theory and Experiment **2005**, P04010 (2005).
- [39] A. Clauset, C. R. Shalizi, and M. E. J. Newman, SIAM Review **51**, 661 (2009), <https://doi.org/10.1137/070710111>.
- [40] Z. Wang, M. Foss-Feig, and K. R. A. Hazzard, arXiv e-prints, arXiv:2009.12032 (2020), arXiv:2009.12032 [quant-ph].
- [41] M. Foss-Feig, Z.-X. Gong, C. W. Clark, and A. V. Gorshkov, Phys. Rev. Lett. **114**, 157201 (2015).
- [42] ITensor Library (version 2.0.11) <http://itensor.org>.

Appendix A: Periodic vs. open boundaries

In this section, we demonstrate how the spin operator (longitudinal magnetization per site) in the middle of an open chain exhibits exponential decay comparable with a spin operator at an arbitrary site in a periodic chain. Fig. 11 compares the nonequilibrium responses of these two spins and as observed, the responses match with each other until the finite-size effects appear. This is reasonable, because a spin in the middle of the chain is equally distant to both edges, and hence it should exhibit behavior closest to a spin in a periodic chain. Therefore, based on this equivalence we can argue that the middle spin of an open chain behaves similar to total magnetization in exhibiting an exponential decay. This is simply because the total magnetization is a sum over all spin operators σ_i^z .

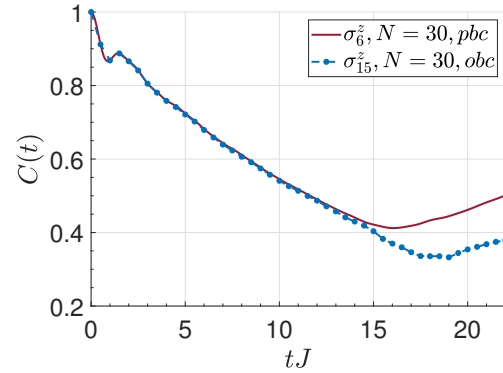


FIG. 11. $C(t)$ nonequilibrium response of the middle spin of an open chain $N = 30$, σ_{15}^z (blue-dotted) and a spin at an arbitrary location σ_6^z in a periodic chain $N = 30$ (red-solid).

Appendix B: Vanishing dynamical order for one-point observables

Here we compare the nonequilibrium responses of a one-point observable and an OTOC, defined at the same site, middle of the chain and quenched from a polarized state $|\psi_0\rangle = |\uparrow\uparrow \dots \uparrow\rangle$. OTOC is defined as, $F(t) = \langle \psi_0 | \sigma_r^z(t) \sigma_r^z(t) \sigma_r^z(t) \sigma_r^z(t) | \psi_0 \rangle$.

Fig. 12a compares $F(t)$ and $C(t)$ for different system sizes N computed via time-dependent density matrix renormalization group (t-DMRG) at transverse field $h/J = 0.5$ in a time interval of $t = N$. When we apply a temporal cutoff of $t = N$, for OTOC, we observe that the

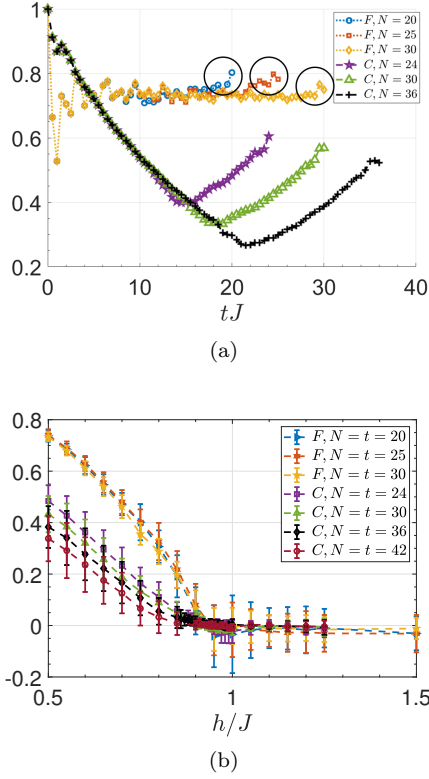


FIG. 12. (a) One-point observable $C(t)$ and OTOC $F(t)$, both defined at a single site, for different system sizes N for integrable TFIM at $h/J = 0.5$; (b) A system-size dependent temporal cutoff is applied to $C(t)$ and $F(t)$ for a time interval of $t = N$ resulting in \bar{C} and \bar{F} with respect to control parameter h/J .

dynamical order persists indefinitely resulting in a well-defined dynamical phase boundary for the time-average or long-time saturation value \bar{F} in Fig. 12b. Note that at $t \sim N$, $F(t)$ in Fig. 12a starts to demonstrate finite-size effects, illustrated with black circles, which justifies the argument that $t \sim N$ is a sufficiently long-time limit $t \rightarrow \infty$ for chosen system sizes. With the same reasoning, one can plot $C(t)$ in a time interval of $t = N$ in Fig. 12a and observe the decay of initial magnetization which dramatically becomes more pronounced as the system size increases, resulting in featureless long-time dynamics as well as a vanishing DPT-I boundary for \bar{C} as seen in Fig. 12b. The error bars in Fig. 12b are 1σ standard deviation of the nonequilibrium response in time (due to oscillations) around the average of the response.

Appendix C: Comparison between fixed and parametric temporal cutoffs

In this section, we plot the difference between rescaled observable values with different choices of temporal cutoffs: (i) fixed α and parametric $2\alpha/v_q$ (ii) two fixed cutoffs in integrable TFIM. Even though these are clearly

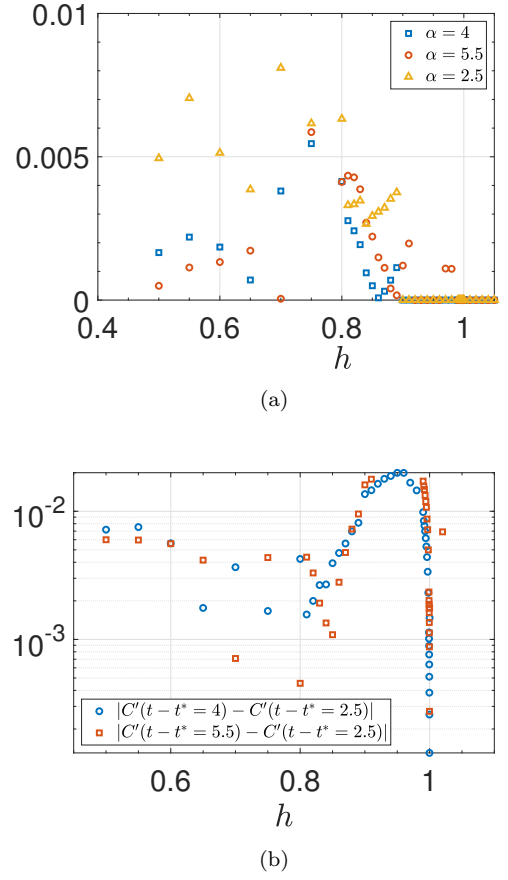


FIG. 13. (a) The differences between rescaled observables with two different temporal cutoffs, parametric $2\alpha/v_q$ and fixed α for different α values (see legend). (b) The differences between rescaled observables with two different fixed temporal cutoffs (see legend).

distinct temporal cutoffs, the differences are bounded for all h/J values in the dynamically-ordered regime and more importantly the differences steadily decrease as we approach the crossover boundary. Fig. 13a demonstrates the differences between rescaled observable values generated with two types of temporal cutoffs for different α values. They are zero at the vicinity of the crossover. This is likely because two types of temporal cutoffs converge to each other as we approach the crossover boundary. Fig. 13b shows the differences between rescaled observable values for two fixed temporal cutoffs. In Fig. 3 in the main text, these differences seem to be the largest and we explained the reason based on how well the numerics can model the exponential decay. Here we explicitly plot the differences and show that the differences steadily decrease as we approach the crossover boundary.

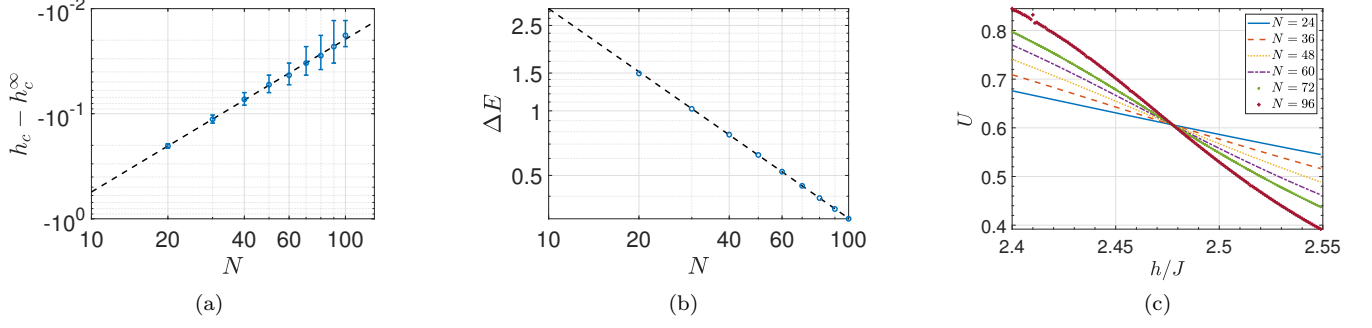


FIG. 14. (a-b) Ground state energy gap analysis with respect to system size N to determine the equilibrium quantum phase boundary. (a) The critical point is marked as $h_c^\infty = 2.463$ in thermodynamic limit via scaling analysis. (b) Energy gap ΔE closes as we approach the QPT boundary. The scaling exponent is $\Delta E = N^{-1}$. (c) Binder cumulant U for different system sizes ranging between $N = 24 - 96$, all crossing at $h_c = 2.477 \pm 0.001$.

Appendix D: Equilibrium QPT boundary for the nonintegrable TFIM

In this section, we present the equilibrium phase transition boundary via both an analysis of ground state energy gap and Binder ratio for the nonintegrable TFIM with $\Delta/J = -1$. Figs. 14a-14b shows the determination of the phase boundary via energy gap analysis. We find that the equilibrium transition happens at $h_c \sim 2.463$ and the scaling exponent of the energy gap closing is $\delta \sim -1$. Further, we compute the Binder cumulant in Fig. 14c,

$$U = \frac{3}{2} \left(1 - \frac{1}{3} \frac{\langle S_z^4 \rangle}{\langle S_z^2 \rangle^2} \right), \quad (\text{D1})$$

where $S_z = \sum_i^N \sigma_i^z$, the total magnetization operator. This method marks the phase boundary as $h_c^\infty = 2.477 \pm 0.001$. The equilibrium transition boundaries determined by these two different methods are very close.

Appendix E: Error bar calculations

The error bars in Figs. 3 and 10 are calculated via error propagation and in Figs. 2, 4 and 8, they are 1σ error bars computed via the confidence intervals of the fittings.

C_0 is fixed parameter in Eq. (3). In the case one uses γ_1 parameter in the rescaling expression instead of $C(t^*)$ data, the free parameter γ_1 brings an uncertainty of $\Delta\gamma_1$ that can be computed via the confidence intervals of the fitting. Based on the data points, one can have an uncertainty from t_L too: Δt denotes this uncertainty which is calculated as the difference between t_L and the available data point. Hence, we can calculate the propagation of error as,

$$E^2 = \left(\frac{\partial \text{OP}}{\partial t} \right)^2 (\Delta t)^2 + \left(\frac{\partial \text{OP}}{\partial \gamma_1} \right)^2 (\Delta \gamma_1)^2, \quad (\text{E1})$$

where OP stands for rescaled observable, or in other words the dynamical OP-like quantity. Note that if one uses the rescaling method (i) for nonintegrable TFIM, additional terms should be added to the expression. The terms in the expression above reads

$$\begin{aligned} \frac{\partial \text{OP}}{\partial \gamma_1} &= -\frac{C(t)^{1/t}}{t} \gamma_1^{-1/t-1}, \\ \frac{\partial \text{OP}}{\partial t} &= -t^{-2} \left(\frac{C(t)}{\gamma_1} \right)^{1/t} \log \left(\frac{C(t)}{\gamma_1} \right). \end{aligned}$$

The error propagation also explains the reason of large error bars in Fig. 10 in main text. These error bars mainly stem from the large error bars of the fitting parameters when we model the dynamic response via minimal model with our limited available data.